



HAL
open science

A hydrogen-dependent geochemical analogue of primordial carbon and energy metabolism

Martina Preiner, Kensuke Igarashi, Kamila Muchowska, Mingquan Yu, Sreejith J. Varma, Karl Kleinermanns, Masaru K. Nobu, Yoichi Kamagata, Harun Tüysüz, Joseph Moran, et al.

► To cite this version:

Martina Preiner, Kensuke Igarashi, Kamila Muchowska, Mingquan Yu, Sreejith J. Varma, et al.. A hydrogen-dependent geochemical analogue of primordial carbon and energy metabolism. *Nature Ecology & Evolution*, 2020, 4 (4), pp.534-542. 10.1038/s41559-020-1125-6 . hal-03024700

HAL Id: hal-03024700

<https://hal.science/hal-03024700>

Submitted on 25 Nov 2020

HAL is a multi-disciplinary open access archive for the deposit and dissemination of scientific research documents, whether they are published or not. The documents may come from teaching and research institutions in France or abroad, or from public or private research centers.

L'archive ouverte pluridisciplinaire **HAL**, est destinée au dépôt et à la diffusion de documents scientifiques de niveau recherche, publiés ou non, émanant des établissements d'enseignement et de recherche français ou étrangers, des laboratoires publics ou privés.

A hydrogen dependent geochemical analogue of primordial carbon and energy metabolism

Martina Preiner^{1,8}, Kensuke Igarashi^{2,8}, Kamila B. Muchowska^{3,8}, Mingquan Yu^{4,8}, Sreejith J. Varma⁵, Karl Kleinermanns⁶, Masaru K. Nobu⁷, Yoichi Kamagata⁷, Harun Tüysüz^{4*}, Joseph Moran^{3*}, William F. Martin^{1*}

⁸ These authors contributed equally: Martina Preiner, Kensuke Igarashi, Kamila B. Muchowska, Mingquan Yu

* e-mail: bill@hhu.de; moran@unistra.fr; tueysuez@kofo.mpg.de

¹ Institute of Molecular Evolution, University of Düsseldorf, 40225 Düsseldorf, Germany

² Bioproduction Research Institute, National Institute of Advanced Industrial Science and Technology (AIST), 2-17-2-1 Tsukisamu-Higashi, Toyohira-ku, Sapporo, Hokkaido 062-8517, Japan

³ Université de Strasbourg, CNRS, ISIS UMR 7006, F-67000 Strasbourg, France

⁴ Max-Planck-Institut für Kohlenforschung, Kaiser-Wilhelm-Platz 1, 45470 Mülheim an der Ruhr, Germany

⁵ Charité – Universitätsmedizin Berlin, Laboratory "Biochemistry and System Biology of the Metabolism", Charitéplatz 1, 10117 Berlin, Germany

⁶ Institute for Physical Chemistry, University of Düsseldorf, 40225 Düsseldorf, Germany

⁷ Bioproduction Research Institute, National Institute of Advanced Industrial Science and Technology (AIST), 1-1-1 Higashi, Tsukuba, Ibaraki 305-8566, Japan

Keywords: Origin of life, serpentinization, hydrothermal vents, early Earth, abiotic carbon fixation, protometabolism, geochemical catalysis.

28 **Editorial Summary**

29 Three iron minerals found in alkaline hydrothermal vents are shown to convert CO₂ and H₂
30 into formate, acetate and pyruvate in water, suggesting that such reactions could have paved
31 the way for early metabolism.

32

33 **Abstract**

34

35 Hydrogen gas, H₂, is generated by alkaline hydrothermal vents through an ancient geochemical
36 process called serpentinization in which water reacts with iron containing minerals deep within
37 the Earth's crust. H₂ is the electron donor for the most ancient and the only energy releasing
38 route of biological CO₂ fixation, the acetyl-CoA pathway. At the origin of metabolism, CO₂
39 fixation by hydrothermal H₂ within serpentinizing systems could have preceded and patterned
40 biotic pathways. Here we show that three hydrothermal minerals—greigite (Fe₃S₄), magnetite
41 (Fe₃O₄) and awaruite (Ni₃Fe)—catalyse the fixation of CO₂ with H₂ at 100°C under alkaline
42 aqueous conditions. The product spectrum includes formate (up to 200 mM), acetate (up to 100
43 μM), pyruvate (up to 10 μM), methanol (up to 100 μM), and methane. The results shed light on
44 both the geochemical origin of microbial metabolism and on the nature of abiotic formate and
45 methane synthesis in modern hydrothermal vents.

46

47 Organic synthesis in hydrothermal vents is relevant to life's origin because the reactions involve
48 sustained energy release founded in the disequilibrium between CO₂ and the vast amounts of
49 molecular hydrogen, H₂, generated in the Earth's crust during serpentinization¹⁻⁹. Hydrogen has
50 been a source of electrons and energy since there was liquid water on the early Earth and it
51 fuelled early anaerobic ecosystems in the Earth's crust^{1,8,10}. In biochemistry, the acetyl-CoA
52 pathway of CO₂ fixation uses the electrons and energy of H₂ to simultaneously supply three key
53 requirements for life: reduced carbon in the form of acetyl groups, electrons in the form of
54 reduced ferredoxin, and ion gradients for energy conservation in the form of ATP^{11,12}. The
55 pathway is linear, not cyclic, it releases energy rather than requiring energy input and its
56 enzymes are replete with primordial metal cofactors^{13,14}. It traces to the last universal common
57 ancestor¹⁵ and abiotic, geochemical organic syntheses resembling segments of the pathway
58 occur in hydrothermal modern vents^{2,3}. Laboratory simulations of the acetyl-CoA pathway's
59 reactions include the nonenzymatic synthesis of thioesters from CO and methylsulfide¹⁶, the
60 synthesis of acetate¹⁷ and pyruvate¹⁸ from CO₂ using native iron or external electrochemical

61 potentials¹⁹ as the electron source. Enzymatic versions of those abiotic reactions occur in core
62 energy metabolism of acetogens and methanogens¹¹⁻¹⁴, ancient anaerobic autotrophs that live
63 from H₂ and CO₂ via the acetyl-CoA pathway and that still inhabit the crust today¹⁴. Though
64 the enzymes that catalyse the modern microbial reactions are well investigated¹¹⁻¹⁴, the catalysts
65 promoting the abiotic reactions in vents today, and that might have been instrumental at life's
66 origin, are poorly understood². A fully abiotic analogue of the acetyl-CoA pathway from H₂
67 and CO₂ as it occurs in life has not been reported to date.

68

69 To probe the mechanisms of hydrothermal metabolic reactions emulating ancient pathways, we
70 investigated three different iron minerals that naturally occur in hydrothermal systems: greigite
71 (Fe₃S₄), magnetite (Fe₃O₄), and the nickel iron alloy awaruite (Ni₃Fe). Magnetite (Fe₃O₄) and
72 awaruite (Ni₃Fe) are common constituents of serpentinizing systems²⁰ and are more stable
73 under alkaline conditions than greigite^{21,22}. Fe₃O₄, like H₂, is a main end product of
74 serpentinization, it is formed from water dependent oxidation of iron(II) silicates²³. In chemical
75 industry, iron based materials are the catalysts of choice for diverse industrial processes
76 including Haber-Bosch (fixation of N₂) and Fischer-Tropsch syngas (CO and H₂) conversion
77 to hydrocarbons⁷. Ni₃Fe is an intermetallic compound that forms in serpentinizing systems at
78 high H₂ partial pressures and very low H₂S fugacities^{5,20}, via the reduction of iron(II) and
79 nickel(II) compounds. It is common in Ni-containing serpentinizing systems, where it is usually
80 deposited as small grains²⁰. Fe₃S₄ is formed under conditions of high H₂S activity^{5,21}, as a
81 transient intermediate in the conversion of mackinawite to pyrite^{22,24}; it shares structural
82 similarity with the iron sulfur clusters of many modern enzymes⁶. Iron sulfides can be found at
83 the surface of hydrothermal vents as small compartments²¹ or as nanoparticles in hydrothermal
84 plumes²⁵ as well as in meteorites²⁶. Iron minerals have long been regarded as ancient
85 catalysts^{6,16,27} although the key initial reaction connecting the inorganic and the organic
86 world—CO₂ fixation with H₂ as the reductant—has not been reported using iron mineral
87 catalysts under biologically relevant conditions¹⁹.

88

89

90 Results

91
92 Although very different in structure and composition (Fig. 1), greigite, magnetite and awaruite
93 are geochemically synthesised in hydrothermal systems from pre-existing divalent iron and
94 nickel minerals during serpentinization^{5,8,28}. X-ray diffraction (XRD) applied to our laboratory
95 preparations of colloidal Fe₃S₄ and Ni₃Fe nanoparticles (for details of synthesis, see Methods)
96 as well as commercial Fe₃O₄ reveals their characteristic patterns of crystal structures (Fig. 1).

97
98 Building on evidence for catalytic reactivity in previous reports^{16–19}, we investigated the ability
99 of greigite, magnetite and awaruite to promote the reduction of CO₂ with H₂ in water. Under
100 very mild hydrothermal conditions—at 100 °C under 2 bar H₂/CO₂ (80:20)—formate and
101 acetate synthesis from H₂ and CO₂ occurs readily in nearly neutral and alkaline aqueous solution
102 in the presence of Fe₃S₄ (Fig. 2a). While only formate was detected at 20 °C, formate and
103 acetate were found at 60 °C, which is close to the temperature of vent effluent (ca. 70°C) in the
104 Lost City hydrothermal field (Fig. 2b)²⁹. At 100 bar, Fe₃S₄ catalyses the synthesis of formate
105 and methane from H₂ and CO₂ (Fig. 2c), but not from CO (Extended Data Fig. 4b). Here,
106 methane and formate production is almost stoichiometric relative to hydrogen decrease. For 14
107 mM H₂ consumed, 1 mM of formate (1 H₂ per molecule of formate) and 2.3 mM of methane (4
108 H₂ per molecule of methane) are produced, leaving only 3.8 mM of H₂ that might go into acetate
109 synthesis (which was below detection in this experimental setup). At 2 bar, formate accumulates
110 to over 2 mM within 4 h, while acetate requires between 4 and 8 h to become detectable (Fig.
111 2d). Notably, formate and methane are the main products of abiotic organic synthesis observed
112 in the effluent of modern serpentinizing hydrothermal systems^{9,30–33}.

113
114 We found that magnetite, like greigite, catalyses the aqueous synthesis of formate and acetate
115 in the range of 10 μM to 1 mM from H₂ and CO₂, but also the formation of methanol and
116 pyruvate under mild (25 bar H₂/CO₂, 40:60 ratio and 100 °C) hydrothermal conditions (Fig.
117 3a). Pyruvate is a crucial intermediate of carbon and energy metabolism in all microbes and the
118 main product of CO₂ fixation in autotrophs that use the acetyl-CoA pathway¹¹. It accumulates
119 at 5–10 μM in the presence of Fe₃O₄ across the pH range of 6–10, when either native iron (Fe)
120 or H₂ is used as the reductant (Fig. 3a). Fe₃O₄ generates a generally uniform product distribution
121 across conditions tested, also when smaller amounts of catalyst are used (Extended Data Fig.
122 6b). Additionally, we investigated different amounts of Fe as a reductant, showing that its

123 impact on product concentrations is low even if a large excess of Fe was used. Both Fe and
124 Fe₃O₄ formed a solid disc after the reaction, which probably hindered further oxidation of Fe
125 and thus further accumulation of reduced carbon compounds (Extended Data Fig. 7a).

126

127 At 100 °C, awaruite catalyses the synthesis of acetate and methanol in the 10–100 μM range at
128 pH 5–8 whereby either the native alloy itself, H₂, or native Fe can function as the reductant,
129 albeit with differing efficiency and product distribution (Fig. 3b). At alkaline conditions, with
130 either native Fe or H₂ as reductant, formate accumulates in the 200 mM range with 1 mmol
131 metal atoms as catalyst. Physical contact between awaruite and native iron is not required for
132 product formation (Extended Data Fig. 7b). In the case of awaruite, lower temperatures
133 improved pyruvate synthesis (Fig. 4a), similar to previous studies¹⁸. Pyruvate is formed under
134 alkaline conditions at 70 °C (Fig. 4a), even at lower catalyst amounts than previously used (0.5
135 mmol metal atoms), and reaches 10 μM when higher amounts of catalyst are used (Fig. 4b).
136 This suggests that pyruvate production in reactions with smaller amounts of awaruite likely
137 occurs, but is below the detection limit of the ¹H-NMR spectroscopy used here. Using even less
138 Ni₃Fe (0.05 mmol metal atoms) is still effective for formate, acetate and methanol formation in
139 thermal gradients from 100 °C to 30 °C (Extended Data Fig. 6a and c), conditions similar to
140 those of natural alkaline hydrothermal vents³⁴. Catalysts are required for the reaction, controls
141 without catalysts yielded only trace levels of product (Extended Data Fig. 2b and c and
142 Supplementary Tabs. 6 and 7).

143

144 In some experiments using Ni₃Fe, we detected ethanol in concentrations up to over 100 μM
145 (Extended Data Fig. 5b). We observed trace amounts of methane (ca. 19 ppm) in awaruite
146 catalysed reactions (Extended Data Fig. 8), which is substantially less than detected in an earlier
147 report using H₂ and CO₂ for 1–2 weeks at 500 bar and 200–400 °C with awaruite as the
148 catalyst³⁵. The hydrothermal conditions we found for the synthesis of organics from H₂ and
149 CO₂ over 16 hours with awaruite as catalyst are mild enough in terms of temperature and
150 energetics to permit microbial growth. Of the catalysts employed, only awaruite showed minor
151 alteration after reaction, probably due to mild oxidation (Fig. 1g–i). Formate accumulation
152 catalysed by awaruite reflects the near-equilibrium interconversion of H₂-CO₂ and formate³⁶.

153

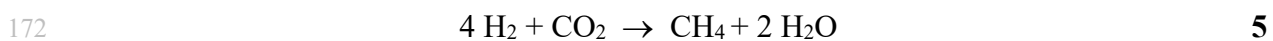
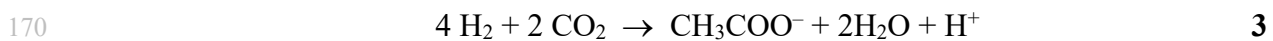
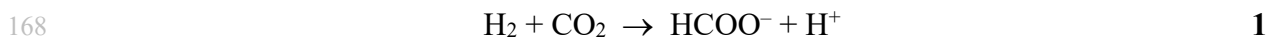
154 To avoid contamination, no organic buffers were employed in any of our experiments. Because
155 Fe₃S₄ is sensitive to high pH, phosphate buffer was employed when greigite was the catalyst.

156 In the experiments with magnetite and awaruite, no buffers were used. In Figs. 3 and 4, blue
157 bars indicate reactions where the starting pH was ~11 through addition of KOH to generate
158 alkaline vent conditions; the pH measured at completion depends on the amount of utilised
159 mineral and metal in addition to the amount of CO₂ dissolved and organic acid synthesised. No
160 water loss, which would potentially distort the product concentrations, was detected in any of
161 our experiments.

162

163 Sustained synthesis of reactive organic compounds was essential at the origin of metabolism
164 and had to be thermodynamically favourable. Equations 1–5 show the redox reactions taking
165 place between CO₂ and H₂ to form formate (1), methanol (2), acetate (3), pyruvate (4), and
166 methane (5).

167



173

174 The changes in Gibbs free energy, ΔG , for six of the H₂-dependent reactions reported here are
175 given in Table 1 (detailed datasets are shown in Supplementary Tabs. 2 and 3). The synthesis
176 of observed products is close to equilibrium or exergonic. For most compounds and conditions,
177 product generation did not reach equilibrium, indicating kinetic inhibition of the reactions. Only
178 H₂-dependent reduction of CO₂ to formate approached equilibrium in the presence of greigite
179 or awaruite (according experiments in Fig. 2a and 3b). Pyruvate and CH₄ production were only
180 detected under specific conditions despite being exergonic in nearly all treatments. For
181 example, in treatments with H₂ and magnetite, pyruvate generation was only detected under
182 alkaline conditions (Fig. 3a), while in treatments with H₂ and awaruite, pyruvate generation
183 was only detected under alkaline conditions and when the amount of mineral was increased
184 (Fig. 4a). H₂-dependent reduction of formate to acetate (eq. 3 – eq. 1; $3\text{H}_2 + \text{CHOO}^- + \text{CO}_2 \rightarrow$
185 $\text{CH}_3\text{COO}^- + 2 \text{H}_2\text{O}$) consistently reached similar ΔG values for each mineral regardless of pH
186 and mineral amount (roughly -72 kJ mol^{-1} for greigite, -89 kJ mol^{-1} for magnetite, and -115

187 kJ mol⁻¹ for awaruite at 100 °C), suggesting the possibility of shared features between the
188 minerals' catalytic mechanisms. None of the three minerals catalyses acetate synthesis to
189 completion ($\Delta G \ll 0$), suggesting the possible presence of kinetic barriers and an opportunity
190 for energetic coupling. For those reactions in which no H₂ was added, only native metals were
191 available as reductant (Extended Data Figs. 3, 5a and 7), likely generating intermediate H₂ from
192 water.

193

194

195 Discussion

196
197 When greigite, magnetite or awaruite are used as catalysts, the synthesis of formate, acetate,
198 methanol and pyruvate from H₂ and CO₂ under hydrothermal conditions is facile. The synthesis
199 of formate and acetate is furthermore robust to the catalyst employed. The main product we
200 observed is formate (Figs. 2–4), which is also the main organic product of abiotic organic
201 synthesis found in alkaline hydrothermal vent effluent^{9,31,37,38}. We propose a mechanism for the
202 catalysed two-electron reduction of CO₂ to formate for all three minerals (Extended Data Fig.
203 10).

204
205 Formate synthesis from H₂ and CO₂ was anticipated by earlier studies^{39,40}, and formate
206 synthesis from CO₂ has been reported at high temperatures (>250 °C) and pressures (>300 bar)
207 with hydrothermal minerals⁴¹. But the amounts of formate that we observe with Ni₃Fe at
208 moderate temperature and pressure (70°C to 100 °C in 25 bar H₂/CO₂ atmosphere), as well as
209 the accumulation of acetate and pyruvate reveal an unexpected correspondence between the
210 spontaneous H₂-dependent CO₂ reduction and metabolism. We see a clear tendency of Ni
211 containing compounds to preferentially produce formate in high concentrations¹⁸, while
212 pyruvate accumulation is preferentially observed with Fe. These product-catalyst specificities
213 are reflected in the active site metals of the corresponding enzymes of the modern acetyl-CoA
214 pathway^{11–13,42–47}.

215
216 Under physiological conditions, the reducing power of H₂ is insufficient to reduce CO₂.
217 Microbes studied so far reduce CO₂ with electrons from H₂ employing flavin-based electron
218 bifurcation to synthesise reduced iron sulfur clusters in ferredoxin for CO₂ fixation^{12,48}. This
219 biological CO₂ fixation usually also entails ion gradients^{48,49}. The reactions reported here
220 require neither electron bifurcation nor ion gradients. With suitable inorganic catalysts that
221 activate both H₂ and CO₂ to enable their reaction, products of the acetyl-CoA pathway (Fig. 2,
222 3 and 4) are formed without the addition of organic cofactors.

223
224 With the exception of ethanol, the reaction products we observe correspond exactly to those of
225 the biological acetyl-CoA pathway to pyruvate¹¹ (Fig. 5). No other reaction products were
226 observed. That is, the mineral catalysed H₂-dependent reduction of CO₂ delivers a very discrete
227 subset of the possible chemical structures: one that constructs the backbone of carbon and

228 energy metabolism in primitive anaerobic autotrophs^{11–15}. The acetyl-CoA pathway^{11,14} entails
229 eleven main enzymes totalling ~15,000 amino acid residues^{13,42–46} plus six organic cofactors
230 each with its own complex biosynthesis¹⁴. The bacterial and archaeal versions of the pathway
231 involve evolutionarily unrelated enzymes but chemically similar methyl synthesis routes^{6,11,14}.
232 The reactions of the acetyl-CoA pathway employed by modern metabolism (Fig. 5) involve the
233 stepwise conservation of chemical energy during CO₂ fixation as acetyl-nickel, acetyl-thioester,
234 acetyl-phosphate, and ATP synthesis via substrate level phosphorylation (marked with an
235 asterisk in Fig. 5)^{11–14}. Although the nature of the catalyst bound intermediates of the biological
236 pathway from H₂ and CO₂ to methane, acetate and pyruvate is known^{11–14}, the identity of the
237 catalyst-bound intermediates of the mineral catalysed reactions is not.

238
239 Proposals for the nature of primordial CO₂ fixation and energy conservation at biochemical
240 origins typically posit the participation of external energy sources⁵⁰ such as UV light⁵¹, heat,
241 impact, pressure, electrical currents, or ion gradients²⁸ to push organic synthesis forward. The
242 reactions reported here require no additional energy source for a protometabolic acetyl-CoA
243 pathway to unfold from H₂ and CO₂ other than the natural reactivity of two gasses and metal
244 catalysts, indicating that neither membranes, though essential for the emergence of free-living
245 cells^{6,52–54}, nor external potentials^{19,55} were required for primordial CO₂ fixation along an
246 exergonic, H₂-dependent, nonenzymatic pathway to C₃ products. The energy for the synthesis
247 of compounds capable of phosphorylating ADP via substrate level phosphorylation^{6,11,12}—for
248 reactions reported here, and for those of the enzymatically catalysed acetyl-CoA pathway—
249 stems from the exergonic synthesis of biologically relevant organic compounds from H₂ and
250 CO₂. Our findings suggest that abiotic, geochemical versions of the energy releasing reactions
251 underlying the acetyl-CoA pathway very likely preceded the enzymes that catalyse it
252 today^{11,14,18,56}. The simplicity and primordial nature of these reactions furthermore suggests that
253 metabolism elsewhere could initiate by a similar route.

254

255 **Methods**

256

257 **General information.** An overview of the performed experiments can be found in Extended
258 Data Fig. 1, and relevant controls – in Extended Data Figs. 2 and 3 and Supplementary Tabs.
259 4–7. The quantity of each transition metal reagent tested as carbon fixation catalyst was
260 normalised to contain the same number of mmol of metal atoms across the experiments. For
261 example, “1 mmol metal atoms” corresponds to: 0.33 mmol greigite Fe_3S_4 (99 mg), 0.33 mmol
262 magnetite Fe_3O_4 (77 mg), and 0.25 mmol awaruite Ni_3Fe (58 mg). Each reaction was performed
263 in at least triplicate. Information on suppliers, grade and purity of all used reagents are listed in
264 the Supplementary Information.

265

266 **Synthesis of greigite (Fe_3S_4).** Every piece of apparatus used in greigite synthesis was stored in
267 an anaerobic chamber (Coy Laboratory Products) under a gas mixture of $\text{N}_2/\text{H}_2/\text{CO}_2$ (80:5:15)
268 for at least 48 h before use, to remove the residual oxygen. Reagents for greigite synthesis were
269 purged with N_2 before use unless otherwise stated. Amorphous $\text{FeO}(\text{OH})$ was synthesised as
270 reported previously⁵⁷ and suspended in Milli-Q water (0.30 mol/L) under air atmosphere. After
271 purging with N_2 , this suspension was stored in a glass bottle under $\text{N}_2/\text{H}_2/\text{CO}_2$ (80:5:15). The
272 solutions of Na_2S (1.0 M) and H_2SO_4 (2.0 M) were prepared as reported previously⁵⁸ and stored
273 in a glass bottle under N_2 . Greigite was synthesised in a solid-gas reaction system as reported
274 previously⁵⁸ with slight modifications. In brief, amorphous $\text{FeO}(\text{OH})$ (0.66 mmol, 2.2 mL of
275 water suspension) was aliquoted to a glass reaction vessel, and a test tube containing 1.0 mL of
276 the Na_2S solution was placed in the vessel inside the anaerobic chamber. The vessel was sealed
277 with an ETFE-coated butyl rubber stopper and an aluminium seal. Then, the vessel was
278 removed from the anaerobic chamber and the headspace gas was replaced with Ar. After
279 returning the vessel into the anaerobic chamber, H_2S gas was generated inside the vessel by
280 injecting 0.5 mL of the H_2SO_4 solution to the Na_2S solution in the test tube using a disposable
281 Myjector syringe (Terumo). The vessel was incubated at 80 °C for 3 hours. The resulting
282 greigite suspension was collected by pipetting from several reaction vessels, washed with 0.5
283 M HCl and then rinsed with N_2 -purged Milli-Q water in the anaerobic chamber as described
284 previously⁵⁸.

285

286 **CO_2 fixation catalysed by greigite.** Synthesised greigite (0.33 mmol) was resuspended in 3 mL
287 of potassium phosphate buffer (20 mM) of a designated pH. The greigite suspension was placed

288 in a fresh glass reaction vessel, which was then sealed with an ETFE-coated butyl rubber
289 stopper and an aluminium seal. The vessel was then removed from the chamber, and the
290 headspace gas was replaced with H₂/CO₂ (80:20) or CO₂ outside the chamber. The vessels were
291 incubated at 100 °C over 4 to 24 h.

292

293 **HPLC analysis (greigite experiments).** Liquid phase components were analysed on a D-2000
294 LaChrom Elite HPLC system (Hitachi), equipped with Aminex[®] HPX-87H column (300 mm,
295 7.8 mm I.D.; Bio-Rad Laboratories) and an L-2400 UV detector at 240 nm and L-2490 RI
296 detector as described previously⁵⁹. Supernatants obtained in the CO₂ reduction experiments
297 were collected after centrifugation inside the anaerobic chamber. 10 µL of the obtained
298 supernatants were directly injected into the HPLC circuit and chromatographed under an
299 isocratic flow of 0.7 mL/min (Eluent: 10 mM H₂SO₄ in H₂O). The column temperature was
300 maintained at 50 °C. Identities of the detected analytes were determined by the LC-MS system:
301 Agilent 1200 HPLC (Agilent Technologies) coupled to an HCT Ultra mass spectrometer
302 (Bruker Daltonics), using a Shodex[®] HILICpak VG-50 2D column (150 mm, 2 mm I.D.; Showa
303 denko). The supernatant prepared as above was mixed with an equal amount of the eluent. Then,
304 5 µL of the mixture was injected into the HPLC circuit and chromatographed under an isocratic
305 flow of 0.1 mL/min (Eluent: a mixture of acetonitrile and 0.25% ammonia water with 80:20
306 ratio). Column temperature was maintained at 30 °C.

307

308 **High-pressure measurements (greigite experiments).** A previously developed⁶⁰ high-pressure
309 incubation system was utilised for the high-pressure CO₂ (Fig. 2c) and CO (Extended Data Fig.
310 4b) reduction reactions in this study. The system consisted of an incubation vessel (stainless
311 steel with Sulfinert[®] coating on its internal wall, volume 150 cm³; Swagelok), inflow/outflow
312 tubes with valves (Swagelok), and a 500D automated syringe pump (Teledyne Isco). The
313 greigite suspension was placed in the reaction vessel inside the anaerobic chamber. After
314 sealing the vessel with inflow and outflow tubes, the headspace gas was replaced with H₂+CO₂
315 (80:20) through a rubber septum equipped with an inflow tube, via a needle. This vessel was
316 then connected to the syringe pump via the inflow tube to complete the incubation system.
317 Potassium phosphate buffer was injected by the syringe pump to reach a hydrostatic pressure
318 of 100 bar. Incubation at 60°C started after H₂ and CO₂ were completely dissolved in the liquid
319 phase (verified by GC analysis). Samples were periodically collected via the outflow tube while
320 keeping the same hydrostatic pressure through automated pressure control of the syringe pump.

321

322 **Gas analysis (greigite experiments).** Gas phase measurements were carried out on a gas
323 chromatograph GC-2014 (Shimadzu) as described previously⁵⁹. Depending on the target gas
324 component, different columns and detectors were used: a Rt-QPLOT (30 m, 0.32 mm I.D, 10
325 μm F.T.; Restek) with flame ionization detector (FID) for CH_4 , molecular sieve 13X column (2
326 m, 3 mm I.D.; Shimadzu) with a thermal conductivity detector (TCD) for H_2 and CO , and
327 activated charcoal column (2.0 m, 3 mm, 60/80 mesh; Shinwa Chemical Industries) with TCD
328 for CO_2 . Pure He and Ar were used as carrier gases for FID and TCD, respectively. The gasses
329 were identified by GC-mass spectrometry (GC-MS) using two systems: 1) TQ8040 NX GC-
330 MS (Shimadzu) equipped with a polar capillary column (TC-70, 30 m, 0.25 mm I.D., 0.25 μm
331 F.T.; GL Sciences); 2) QP2010 Plus GC-MS (Shimadzu) equipped with Rt-Q-BOND (15 m,
332 0.32 mm I.D., 10 μm F.T.; Restek). Carrier gas in both systems was pure He.

333
334 **Synthesis of awaruite (Ni_3Fe) nanoparticles.** As previously reported^{61,62}, spent tea leaves can
335 be used as sustainable hard template to synthesise native metal nanoparticles in the desired
336 composition. For the synthesis of nanoparticulate Ni_3Fe , washed and dried tea leaves were added
337 into an aqueous solution of $\text{Ni}(\text{NO}_3)_2 \cdot 6\text{H}_2\text{O}$ and $\text{Fe}(\text{NO}_3)_3 \cdot 9\text{H}_2\text{O}$ (molar ratio of 3:1) and stirred
338 at room temperature for 2 h. The mass ratio of tea leaves and metal precursors was set at 2:1.
339 Due to the low decomposition temperature of the metal nitrate salt (below 200°C), metal oxide
340 nanoparticles can be formed in the pore confinement of the template before its structural
341 damage/combustion. The carbon-based tea leaf template was burned out in air atmosphere (at
342 550°C for 4 h) and the resulting Ni_3Fe oxide was washed with 0.1 M HCl solution for 2 h and
343 cleaned with deionised water. Finally, the product was treated in a reductive 10% H_2/Ar flow
344 (100 mL/min) at 500°C for 2 h to generate the intermetallic Ni_3Fe compound.

345
346 **CO_2 fixation catalysed by magnetite (Fe_3O_4) and awaruite (Ni_3Fe).** Awaruite and magnetite
347 powder (commercial) were placed in a 1.5 mL glass vial. In the case of magnetite experiments
348 and the awaruite experiments displayed in Fig. 2d, a clean PTFE-coated stir bar was added to
349 the vial. All further awaruite experiments were conducted without stir bars. Then, the reaction
350 vials were filled with 1.0 mL of Milli-Q water. Whenever the effect of an increased pH of the
351 reaction mixtures was tested, solid KOH was added into the Milli-Q water before the reaction
352 (45 mg/mL). KOH had been tested for contaminants via the $^1\text{H-NMR}$ analysis (Extended Data
353 Fig. 9a). To prevent cross-contamination while allowing for the gas to easily reach the reaction
354 mixture, the vials were closed with caps with punctured PTFE septa. The reaction vials (3–12)

355 were placed in a stainless-steel pressure reactor (Berghof or Parr) which was then sealed,
356 flushed three times with ca. 5 bar CO₂, pressurised to a final value of 25 bar CO₂ (unless noted
357 otherwise), and heated at the desired temperature (an external heating mantle was used) for
358 16 h. At a reaction temperature of 100 °C, a maximum pressure of ca. 30 bar was reached. After
359 the reaction, the reactor was allowed to cool down to room temperature (3–4 h from 100 °C, 2–
360 3 h from 70 °C) before sample analysis^{18,56}.

361
362 ***Experiments with iron powder or hydrogen gas.*** The experiments were performed according
363 to the general procedure described above, except that 10 mmol (560 mg) Fe⁰ powder was first
364 placed in the reaction vials, followed by the mineral tested and no stir bars were added. Further
365 experiments exploring the impact of the amount of Fe⁰ powder are displayed in Extended Data
366 Fig. 7a). Whenever H₂ was used in the experiments, the pressure reactor was first flushed with
367 CO₂, then pressurised with 10 bar of H₂ and then brought to 25 bar by adding CO₂ again
368 (H₂/CO₂ approximately 40:60).

369
370 ***Work-up procedure for reaction mixtures (Ni₃Fe and Fe₃O₄).*** The pH of individual reaction
371 mixtures was determined via TRITEST L pH 1–11 pH papers (Macherey-Nagel) directly after
372 the reaction. The values of the Ni₃Fe experiments were confirmed with a pH-Meter (Lab 875,
373 SI Analytics) and a pH combination microelectrode (A 157 IDS, SI Analytics). The CO₂
374 dissolved in the reaction mixture during the reaction decreased the reaction pH values due to
375 the formation of carbonic acid. Reaction mixtures that did not contain KOH were either treated
376 with ca. 45 mg solid KOH per 1 mL reaction mixture to precipitate the metal ions as hydroxides
377 (in the case of Fe₃O₄ and Ni₃Fe experiments displayed in Fig. 3), or left untreated (in the case
378 of Ni₃Fe). The treatment of individual experimental rows was also dependent on the visible
379 concentration of metal ions in solution (since these ions have to be removed by precipitation as
380 hydroxides prior to NMR measurements) and is additionally described in the according figure
381 legends. All samples were then centrifuged at 13.000 rpm for 10 min. The supernatant was then
382 separated from the precipitate (catalyst) and stored at 4 °C overnight or longer until the NMR
383 or HPLC analysis.

384
385 ***NMR analysis (for awaruite and magnetite experiments).*** Concentrations of formate, acetate,
386 pyruvate and methanol (as methoxide) were determined by ¹H-NMR, following the protocol
387 established in Varma et al¹⁸. The supernatant of the centrifuged samples was therefore mixed
388 with sodium 3-(trimethylsilyl)-1-propanesulfonate (DSS) D₂O-solution as the internal standard

389 (CH₃ peak at 0 ppm). NMR spectra were acquired on a Bruker Avance III – 600 or a Bruker
390 Avance 300 spectrometer at 297 K, using a ZGESGP pulse program. 32 scans were acquired
391 for each sample, the relaxation delay was set to 40 s (600 MHz) and 87 s (300 MHz), with a
392 spectral width of 12315 ppm (600 MHz) or 11963 ppm (300 MHz). Analysis and integration
393 were performed using MestReNova (10.0.2) software. Shifts of the measured products are
394 depicted in Extended Data Fig. 9b.

395

396 **Powder X-ray diffraction (XRD).** XRD analysis was performed for pre- and post-reaction
397 catalysts. For greigite, XRD specimen was prepared as described previously⁵⁸. In brief, the
398 sample was collected by centrifugation, and the obtained pellet was directly mounted as a slurry
399 form on a silicon holder (SanyuShoko), and then sealed by using polyimide film (Nilaco
400 Corporation) and vacuum grease (JEOL) to avoid possible desiccation and oxidation during the
401 analysis. The specimen was analysed using a RINT2000 X-ray diffractometer (Rigaku) at room
402 temperature for CuK $\alpha_{1,2}$ radiation scanning at a step interval of 0.02° 2 θ and a counting time
403 of 2 seconds with a 2 θ range from 20° to 60°, operating at an accelerating voltage of 40 kV at
404 30 mA. In order to prepare specimens for magnetite and awaruite experiments, the samples
405 were collected, washed with Milli-Q water and dried under vacuum. XRD patterns of these
406 specimens were collected at room temperature by using a theta-theta diffractometer (Stoe) in
407 Bragg-Brentano geometry for CuK $\alpha_{1,2}$ radiation scanning at a step interval of 0.04° 2 θ and a
408 counting time of 6 seconds with a 2 θ range from 20° to 80°.

409

410 **Electron microscopy.** Electron microscopic observation was conducted for pre-reaction
411 catalysts to check their morphology. For greigite, a specimen for scanning electron microscopy
412 was prepared as described previously⁵⁸. Briefly, in the anaerobic chamber, greigite was rinsed
413 at least three times with N₂-purged Milli-Q water, dried at room temperature, and then mounted
414 on an aluminium stab using carbon tape. The specimen was taken out from the anaerobic
415 chamber, coated with platinum/palladium alloy with an ion sputter E102 (Hitachi) and observed
416 on a JSM-6330F (JEOL) or JSM-7800F (JEOL) field-emission scanning electron microscope
417 (FE-SEM) at an acceleration voltage of 5 kV. The magnetite sample was deposited on lacey
418 carbon film-coated Cu grids (400 mesh), and observed on an H-7100 (Hitachi) transmission
419 electron microscope at an acceleration voltage of 100 kV. The awaruite sample was collected
420 and embedded in Spurr resin (hard mixture). Obtained resin blocks were trimmed using an EM
421 TRIM milling system (Leica). Thin sections were cut from the resin blocks by using a
422 microtome with a 35° diamond knife (Reichert Ultra-Cut), dispersed in Milli-Q water and

423 transferred from the water surface on lacey carbon film-coated Cu grids (400 mesh), and
424 observed on an S-5500 (Hitachi) scanning transmission electron microscope at an acceleration
425 voltage of 30 kV.

426

427 ***Thermodynamic calculations.*** For Gibbs free energy yield (ΔG) calculations, published values
428 of ΔH and ΔG values were used^{63,64}. The effect of temperature on the Gibbs free energy yield
429 was calculated using the Gibbs-Helmholtz equation. Equilibrium constants at different
430 temperatures were adjusted using the van't Hoff equation (detailed equations in the
431 Supplementary Information). Corrections based on non-standard pressures were estimated
432 using partial molar volume changes of the reactions⁶⁵. For any organic compounds that were
433 not detected, an aqueous concentration of 0.1 μM was assumed. For CH_4 , a partial pressure of
434 10^{-7} bar was assumed when not detected. In reactions containing Fe^0 as an electron donor
435 (Supplementary Tab. 2), the H_2 concentration was estimated by assuming H_2 -dependent CO_2
436 reduction to formate reached equilibrium. Final H_2 and CO_2 concentrations were estimated
437 based on the measured products (subtracting 1 mol H_2 per mole formate detected).

438

439

440

441 **Tables**

442

443 **Table 1:** Changes in Gibbs free energy ΔG for the CO₂ fixation product formation
444 in kJ mol⁻¹.

445

446

447

448

449

450

451

452

453

454

Product	Greigite		Magnetite		Awaruite	
	1	2	3	4	5	6
Formate	0.31	-25.58	-19.56	-48.14	-2.56	-15.26
Methanol	ND	ND	-46.60	-46.60	-51.49	-50.33
Acetate	-71.00	-96.69	-108.59	-137.16	-120.03	-132.17
Pyruvate	ND	ND	ND	-57.18	ND	ND

455

Notes:

456

457

458

459

460

461

462

463

464

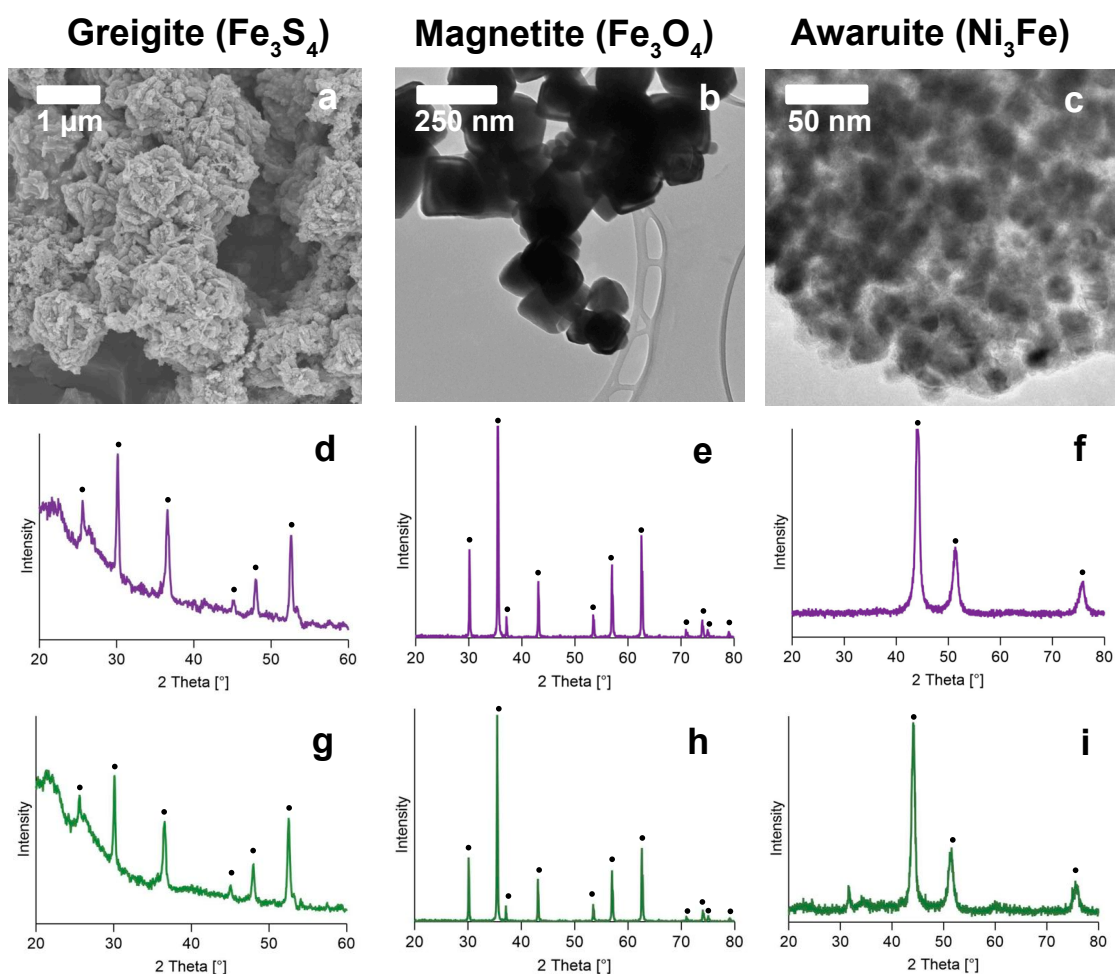
465

466

467

468

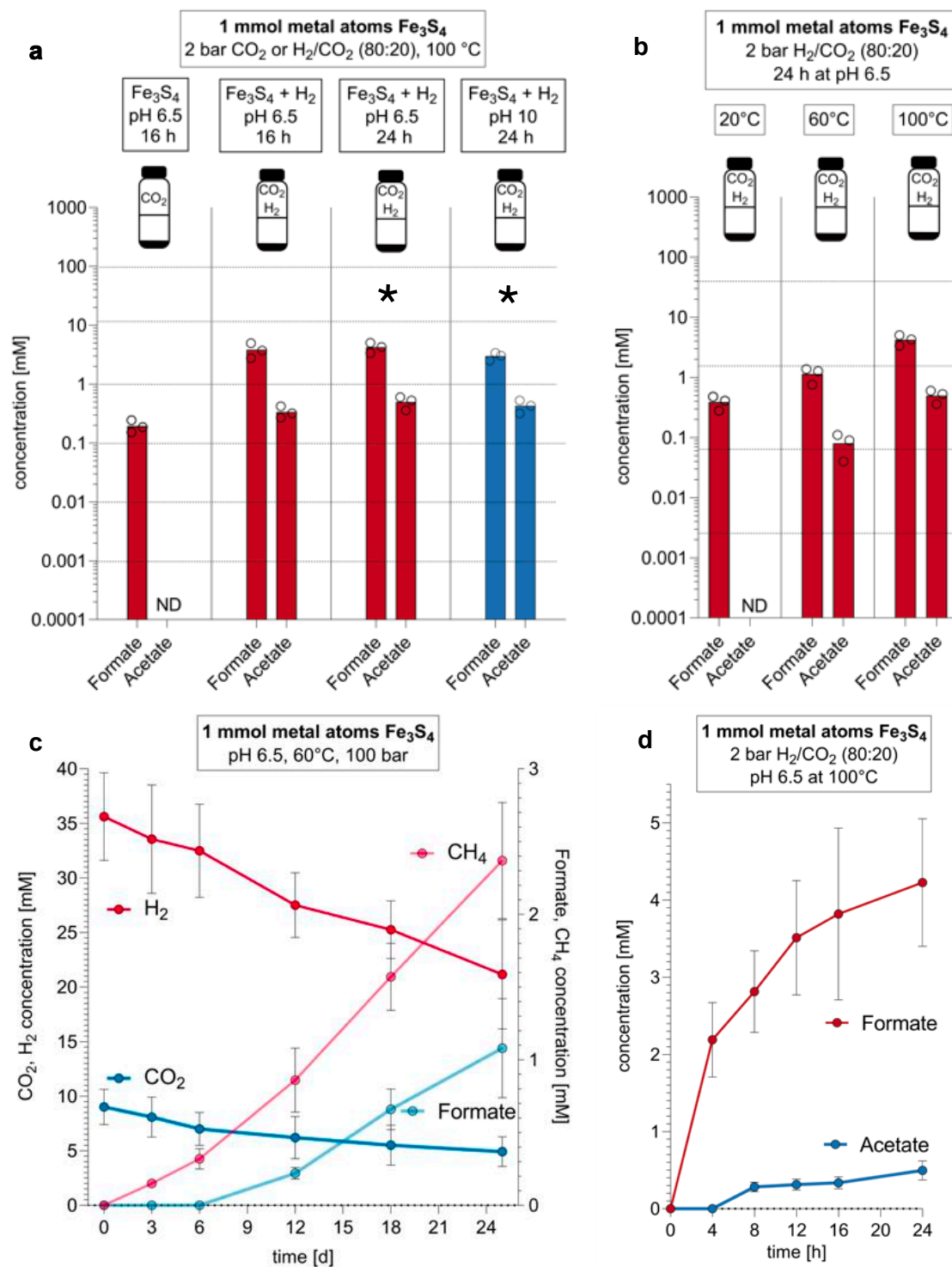
Figures



469

470 **Figure 1:** Characterisation of greigite (Fe_3S_4), magnetite (Fe_3O_4) and awaruite (Ni_3Fe)
 471 catalysts. The three powders are different in structure and morphology as seen from
 472 electron microscopy images (**a**, **b**, **c**), of which greigite and awaruite are freshly
 473 synthesised, magnetite is commercially obtained. Comparison of the XRD patterns of the
 474 minerals before the reaction (**d**, **e**, **f**) and after the experiments under the following
 475 conditions: Fe_3O_4 (**h**) and Ni_3Fe (**i**) for 16 h under alkaline conditions (potassium
 476 hydroxide added) under a H_2/CO_2 atmosphere. Fe_3S_4 (**g**), for 24 h at pH 6.5, stabilised by
 477 a phosphate buffer under a H_2/CO_2 atmosphere.

478

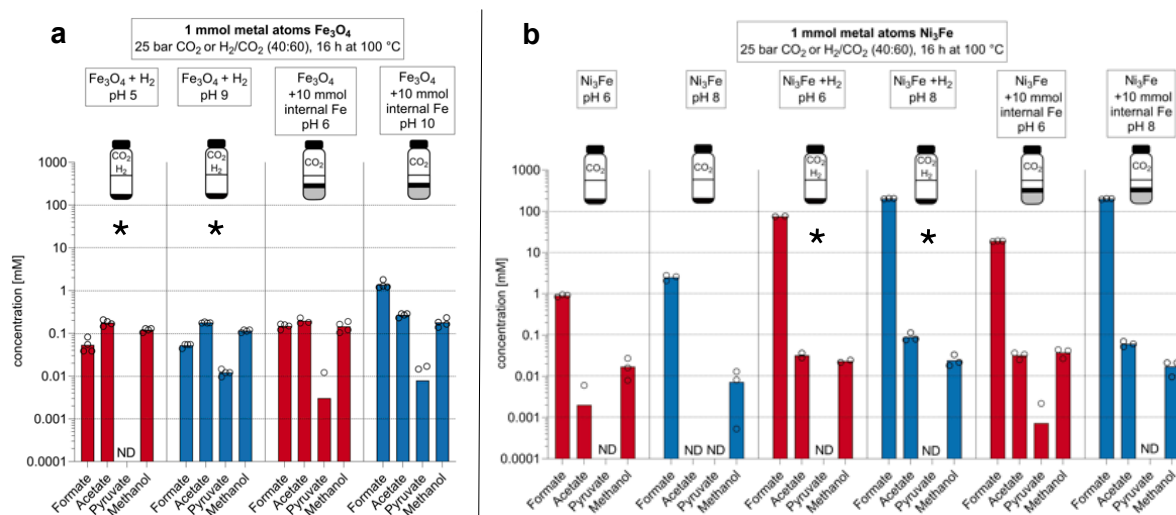


479

480 **Figure 2:** a Fixation of CO_2 with H_2 , catalysed by greigite. b Effect of temperature on
 481 greigite catalysis. c Time course experiment of high-pressure methane and formate
 482 production from CO_2 and H_2 under greigite catalysis (liquid phase, 150 mL) at 100 bar
 483 and 60 °C. (d) Reaction progress over time at a 2 bar H_2/CO_2 atmosphere and 100 °C. All
 484 reactions were performed in water containing a phosphate buffer (3 mL for (a), (b) and
 485 (d), 150 mL for (c)). Flasks in the first two panels summarise the reaction parameters:

486 greigite is depicted in black. Catalyst amounts are normalised by the number of moles of
 487 metal atoms per mole of mineral compound, 0.33 mmol of greigite (Fe_3S_4) are equivalent
 488 to 1 mmol of metal atoms each. Individual experiments were performed under either CO_2
 489 or H_2/CO_2 atmosphere. Red bars: $\text{pH}<7$, Blue bars: $\text{pH}>7$. ND: not detected (no product
 490 was formed or product concentration was below the detection limit). Circles correspond
 491 to the values of individual experiments. Values of 0 are not shown by the logarithmic
 492 scale. Asterisks indicate experiments for which the Gibbs free energy was calculated in
 493 Tab. 1. Concentration values and standard deviations of the experiments are listed in
 494 Supplementary Tab. 1, control experiments are shown in Extended Data Fig. 2a. The
 495 influence of pH (4–10) on the reactions catalysed by greigite is shown in Extended Data
 496 Fig. 4a).

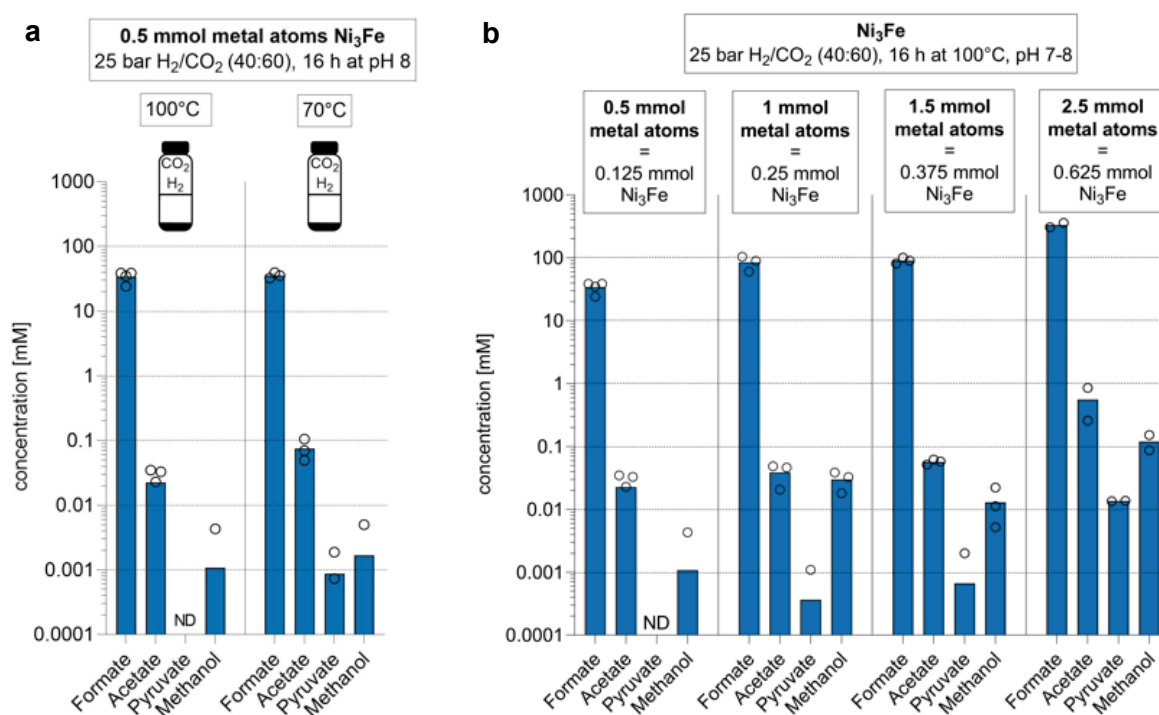
497



498

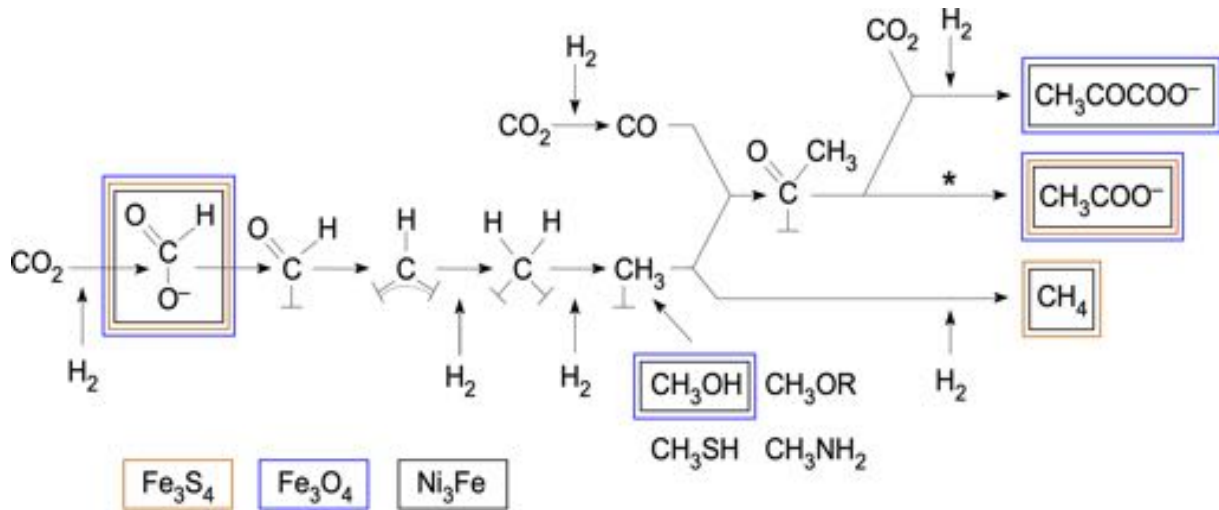
499 **Figure 3:** Fixation of CO_2 with H_2 , catalysed by **a** magnetite and **b** awaruite. All reactions
 500 were performed in water (1 mL). Flasks in each panel summarise the reaction parameters:
 501 hydrothermal minerals are depicted in black, additional iron powder in grey. Catalyst
 502 amounts are normalised by the number of moles of metal atoms per mole of mineral
 503 compound: 0.33 mmol of magnetite (Fe_3O_4), as well as 0.25 mmol of awaruite are
 504 equivalent to 1 mmol of metal atoms in each catalyst. Individual experiments were
 505 performed under either CO_2 atmosphere, H_2/CO_2 atmosphere, or CO_2 atmosphere with Fe
 506 powder as an electron source (also for H_2 formation from H_2O). Experiments without
 507 native Fe were performed with decontaminated stir bars, those containing native Fe were
 508 performed without stir bars due to the solidification of the Fe powder during the process.
 509 Red bars: $\text{pH}<7$, Blue bars: $\text{pH}>7$. ND: not detected (no product was formed or product

510 concentration was below the detection limit). Experiments performed at pH<7 were
 511 treated with KOH after the reaction as in Varma et al.¹⁸. Circles correspond to the values
 512 of individual experiments. Values of 0 are not shown by the logarithmic scale. Asterisks
 513 indicate experiments for which the Gibbs free energy was calculated in Tab. 1.
 514 Concentration values and standard deviations of the experiments are listed in
 515 Supplementary Tab. 1, control experiments are shown in Extended Data Figs. 2b and c
 516 (Ni₃Fe) and 3 (Fe⁰) and Supplementary Tabs. 4–7. Background levels of formate at least
 517 three orders of magnitude below experimental product concentrations (Ni₃Fe);
 518 background levels of acetate (ca. 10 to 20 μM) were observed in controls using Ni₃Fe as
 519 the catalyst. All background levels were subtracted before plotting (see Supplementary
 520 Information for all background values).



521
 522 **Figure 4: a** Effect of temperature on Ni₃Fe catalysis. **b** Impact of Ni₃Fe catalyst amount.
 523 All reactions were performed in water (1 mL). Catalyst amounts are normalised to the
 524 number of moles of metal atoms per mole of mineral compound: 0.25 mmol of awaruite
 525 is equivalent to 1 mmol of metal atoms. Individual experiments were performed under
 526 H₂/CO₂ (40:60) atmosphere. All experiments were conducted without stir bars. Circles
 527 correspond to the values of individual experiments. Values of 0 are not shown by the
 528 logarithmic scale. All measurements were performed in at least triplicate (2.5 mmol Ni₃Fe
 529 in duplicate) ND: not detected (no product was formed or product concentration was

530 below the detection limit). Circles correspond to the values obtained in individual
 531 experiments. Values of 0 are not shown by the logarithmic scale. Concentration values
 532 and standard deviations of the experiments are listed in Supplementary Tab. 1, control
 533 experiments are shown in Extended Data Fig. 2b and c and Supplementary Tabs. 6 and 7.
 534



536 **Figure 5:** Congruence between the acetyl-CoA pathway and reactions catalysed by three
 537 iron minerals found in hydrothermal vents. The chemical reactions summarise the acetyl-
 538 CoA pathway as it occurs in hydrogenotrophic bacteria and archaea as depicted in ref.¹¹,
 539 with the exception of free formate later discovered in the archaeal pathway⁶⁶. The
 540 methenyl (=CH-), methylene (-CH₂-), and methyl (-CH₃) groups of the bacterial and
 541 archaeal pathway are bound to tetrahydrofolate and tetrahydromethanopterin,
 542 respectively, generically indicated as catalysts (⊥) here. Coloured boxes indicate products
 543 observed in reactions using iron mineral catalysts. An asterisk indicates the reaction
 544 sequence in which energy is conserved as ATP via substrate level phosphorylation in the
 545 biological pathway (the acyl-nickel, thioester and acyl-phosphate intermediates that the
 546 enzymatic pathway employs for the stepwise conservation of free energy in the exergonic
 547 conversion of the nickel-bound acyl group to ATP¹¹ are not shown). All products shown
 548 were observed at temperatures ≤100 °C and obtained within <24 h, except methane in the
 549 case of greigite, which was observed over the course of 25 d (Fig. 2c). Methanol, methyl
 550 sulfide, methyl amines, and methoxy groups from coal can serve as methyl donors for the
 551 pathway^{11,67}.

552
 553 **Contributions**

554

555 W.F.M. wrote the initial draft of the main text and all authors edited the manuscript. W.F.M.,
556 H.T., J.M. and M.P. designed the awaruite experiments, M.P. performed the awaruite
557 experiments and assembled the results for the main text and SI material. K.B.M. designed and
558 performed the magnetite experiments, S.J.V. performed exploratory experiments with
559 magnetite. Design of the greigite experiments was done by K.I. and Y.K., K.I. performed the
560 experiments. H.T. and M.Y. designed and synthesised the awaruite nanoparticles and
561 performed XRD and TEM measurements for magnetite and awaruite experiments. M.K.N.
562 performed and interpreted the thermodynamics calculations. K.K., J.M., H.T. and M.P.
563 formulated the H₂ reduction mechanism shown in the SI.

564

565 **Acknowledgements**

566

567 We thank Yitao Dai for setting up gas analysis for the awaruite experiments, Andrey do
568 Nascimento Vieira for performing parts of the revision experiments, Alexander Bähr, and
569 Perlina Lim for scientific support and Joana C. Xavier for discussions. For funding, J.M.,
570 W.F.M. and H.T. thank the VW foundation (96_742). W.F.M. and H.T. thank the Deutsche
571 Forschungsgemeinschaft (MA-1426/21-1 / TU 315/8-1) and W.F.M thanks the European
572 Research Council (ERC 666053). This work is partly supported by IMPRS-RECHARGE and
573 MAXNET Energy consortium of the Max Planck Society. K.I. and Y.K. thank JSPS KAKENHI
574 Grant-in-Aid for Scientific Research on Innovative Areas (K.I.: JP17H05240 / Y.K.:
575 26106004). K.I. is also supported by Grant-in-Aid for Young Scientists B (JP17K15255). J.M.
576 thanks the European Research Council (ERC 639170) and ANR LabEX (ANR-10-LABX-0026
577 CSC). This work was also partly supported by Nanotechnology Platform Program (Molecule
578 and Material Synthesis) of the Ministry of Education, Culture, Sports, Science and Technology
579 (MEXT), Japan.

580

581 **Data Availability Statement**

582 All data are available in the main text, Extended Data Figs. 1–10 and the Supplementary
583 Information (Supplementary Materials and Methods, Supplementary Tables 1–7,
584 Supplementary Figures 1–29 and Supplementary Equations).

585

586 **Competing Interests**

587 The authors declare no competing interests.

588

589 **References**

590

- 591 1. Baross, J. A. & Hoffman, S. E. Submarine hydrothermal vents and associated gradient
592 environments as sites for the origin and evolution of life. *Orig. Life Evol. Biosph.* **15**,
593 327–345 (1985).
- 594 2. McCollom, T. M. Abiotic methane formation during experimental serpentinization of
595 olivine. *Proc. Natl. Acad. Sci. U.S.A.* **113**, 13965–13970 (2016).
- 596 3. McDermott, J. M., Seewald, J. S., German, C. R. & Sylva, S. P. Pathways for abiotic
597 organic synthesis at submarine hydrothermal fields. *Proc. Natl. Acad. Sci. U.S.A.* **112**,
598 7668–7672 (2015).
- 599 4. Ménez, B. *et al.* Abiotic synthesis of amino acids in the recesses of the oceanic
600 lithosphere. *Nature* **564**, 59–63 (2018).
- 601 5. Klein, F. & Bach, W. Fe-Ni-Co-O-S phase relations in peridotite-seawater interactions.
602 *J. Petrol.* **50**, 37–59 (2009).
- 603 6. Martin, W. F. & Russell, M. J. On the origin of biochemistry at an alkaline
604 hydrothermal vent. *Philos. Trans. R. Soc. B Biol. Sci.* **362**, 1887–1925 (2007).
- 605 7. Preiner, M. *et al.* Serpentinization: Connecting geochemistry, ancient metabolism and
606 industrial hydrogenation. *Life* **8**, 41 (2018).
- 607 8. Sleep, N. H., Bird, D. K. & Pope, E. C. Serpentinite and the dawn of life. *Philos.*
608 *Trans. R. Soc. B Biol. Sci.* **366**, 2857–2869 (2011).
- 609 9. Schrenk, M. O., Brazelton, W. J. & Lang, S. Q. Serpentinization, carbon, and deep life.
610 *Rev. Mineral. Geochemistry* **75**, 575–606 (2013).
- 611 10. Arndt, N. T. & Nisbet, E. G. Processes on the young Earth and the habitats of early life.
612 *Annu. Rev. Earth Planet. Sci.* **40**, 521–549 (2012).
- 613 11. Fuchs, G. Alternative pathways of carbon dioxide fixation: Insights into the early
614 evolution of life? *Annu. Rev. Microbiol.* **65**, 631–658 (2011).
- 615 12. Müller, V., Chowdhury, N. P. & Basen, M. Electron bifurcation: A long-hidden
616 energy-coupling mechanism. *Annu. Rev. Microbiol.* **72**, 331–353 (2018).
- 617 13. Ragsdale, S. W. & Pierce, E. Acetogenesis and the Wood-Ljungdahl pathway of CO₂
618 fixation. *Biochim. Biophys. Acta* **1784**, 1873–1898 (2008).
- 619 14. Sousa, F. L. & Martin, W. F. Biochemical fossils of the ancient transition from
620 geoenergetics to bioenergetics in prokaryotic one carbon compound metabolism.
621 *Biochim. Biophys. Acta - Bioenerg.* **1837**, 964–981 (2014).
- 622 15. Weiss, M. C. *et al.* The physiology and habitat of the last universal common ancestor.

- 623 *Nat. Microbiol.* **1**, 16116 (2016).
- 624 16. Huber, C. & Wächtershäuser, G. Activated acetic acid by carbon fixation on (Fe,Ni)S
625 under primordial conditions. *Science* **276**, 245–248 (1997).
- 626 17. He, C., Tian, G., Liu, Z. & Feng, S. A mild hydrothermal route to fix carbon dioxide to
627 simple carboxylic acids. *Org. Lett.* **12**, 649–651 (2010).
- 628 18. Varma, S. J., Muchowska, K. B., Chatelain, P. & Moran, J. Native iron reduces CO₂ to
629 intermediates and endproducts of the acetyl-CoA pathway. *Nat. Ecol. Evol.* **2**, 1019–
630 1024 (2018).
- 631 19. Roldan, A. *et al.* Bio-inspired CO₂ conversion by iron sulfide catalysts under
632 sustainable conditions. *Chem. Commun.* **51**, 7501–7504 (2015).
- 633 20. Rajendran, S. & Nasir, S. Hydrothermal altered serpentized zone and a study of Ni-
634 magnesioferrite–magnetite–awaruite occurrences in Wadi Hibi, Northern Oman
635 Mountain: Discrimination through ASTER mapping. *Ore Geol. Rev.* **62**, 211–226
636 (2014).
- 637 21. Russell, M. J. & Hall, A. J. The emergence of life from iron monosulphide bubbles at a
638 submarine hydrothermal redox and pH front. *J. Geol. Soc. London.* **154**, 377–402
639 (1997).
- 640 22. Rickard, D. & Luther, G. W. Chemistry of Iron Sulfides. *Chem. Rev.* **107**, 514–562
641 (2007).
- 642 23. McCollom, T. M. & Seewald, J. S. Serpentinites, hydrogen, and life. *Elements* **9**, 129–
643 134 (2013).
- 644 24. Hunger, S. & Benning, L. G. Greigite: A true intermediate on the polysulfide pathway
645 to pyrite. *Geochem. Trans.* **8**, (2007).
- 646 25. Findlay, A. J. *et al.* Iron and sulfide nanoparticle formation and transport in nascent
647 hydrothermal vent plumes. *Nat. Commun.* **10**, 1597 (2019).
- 648 26. Schmitt-Kopplin, P. *et al.* High molecular diversity of extraterrestrial organic matter in
649 Murchison meteorite revealed 40 years after its fall. *Proc. Natl. Acad. Sci. U.S.A.* **107**,
650 2763–2768 (2010).
- 651 27. Dayhoff, M. O. & Eck, R. V. Evolution of the structure of ferredoxin based on
652 surviving relics of primitive amino acid sequences. *Science* **152**, 363–366 (1966).
- 653 28. White, L. M., Bhartia, R., Stucky, G. D., Kanik, I. & Russell, M. J. Mackinawite and
654 greigite in ancient alkaline hydrothermal chimneys: Identifying potential key catalysts
655 for emergent life. *Earth Planet. Sci. Lett.* **430**, 105–114 (2015).
- 656 29. Kelley, D. S. *et al.* An off-axis hydrothermal vent field near the Mid-Atlantic Ridge at

- 657 30° N. *Nature* (2001). doi:Doi 10.1038/35084000
- 658 30. Kelley, D. S., Baross, J. A. & Delaney, J. R. Volcanoes, Fluids, and Life at Mid-Ocean
659 Ridge Spreading Centers. *Annu. Rev. Earth Planet. Sci.* **30**, 385–491 (2002).
- 660 31. Lang, S. Q., Butterfield, D. A., Schulte, M., Kelley, D. S. & Lilley, M. D. Elevated
661 concentrations of formate, acetate and dissolved organic carbon found at the Lost City
662 hydrothermal field. *Geochim. Cosmochim. Acta* **74**, 941–952 (2010).
- 663 32. Lang, S. Q. *et al.* Deeply-sourced formate fuels sulfate reducers but not methanogens at
664 Lost City hydrothermal field. *Sci. Rep.* **8**, 755 (2018).
- 665 33. Etiope, G. & Sherwood Lollar, B. Abiotic methane on Earth. *Rev. Geophys.* **51**, 276–
666 299 (2013).
- 667 34. Kelley, D. S. *et al.* An off-axis hydrothermal vent field near the Mid-Atlantic Ridge at
668 30° N. *Nature* **412**, 145–149 (2001).
- 669 35. Horita, J. & Berndt, M. E. Abiogenic methane formation and isotopic fractionation
670 under hydrothermal conditions. *Sci. Rep.* **285**, 1055–1057 (1999).
- 671 36. Schuchmann, K. & Müller, V. Direct and reversible hydrogenation of CO₂ to formate
672 by a bacterial carbon dioxide reductase. *Science* **342**, 1382–1385 (2013).
- 673 37. Eickenbusch, P. *et al.* Origin of short-chain organic acids in serpentinite mud
674 volcanoes of the Mariana convergent margin. *Front. Microbiol.* **10**, 1–21 (2019).
- 675 38. Etiope, G. & Schoell, M. Abiotic gas: atypical, but not rare. *Elements* **10**, 291–296
676 (2014).
- 677 39. McCollom, T. M. & Seewald, J. S. Experimental constraints on the hydrothermal
678 reactivity of organic acids and acid anions: I. Formic acid and formate. *Geochim.*
679 *Cosmochim. Acta* **67**, 3625–3644 (2003).
- 680 40. McCollom, T. M. & Seewald, J. S. Carbon isotope composition of organic compounds
681 produced by abiotic synthesis under hydrothermal conditions. *Earth Planet. Sci. Lett.*
682 **243**, 74–84 (2006).
- 683 41. McCollom, T. M. & Seewald, J. S. A reassessment of the potential for reduction of
684 dissolved CO₂ to hydrocarbons during serpentinization of olivine. *Geochim.*
685 *Cosmochim. Acta* **65**, 3769–3778 (2001).
- 686 42. Menon, S. & Ragsdale, S. W. Unleashing hydrogenase activity in carbon monoxide
687 dehydrogenase/acetyl-CoA synthase and pyruvate:ferredoxin oxidoreductase.
688 *Biochemistry* **35**, 15814–15821 (1996).
- 689 43. Jeoung, J.-H. & Dobbek, H. Carbon dioxide activation at the Ni,Fe-cluster of anaerobic
690 carbon monoxide dehydrogenase. *Conserv. Exhib.* **318**, 1461–1464 (2007).

- 691 44. Dobbek, H., Svetlitchnyi, V., Gremer, L., Huber, R. & Meyer, O. Crystal structure of a
692 carbon monoxide dehydrogenase reveals a [Ni-4Fe-5S] cluster. *Science* **293**, 1281–
693 1285 (2001).
- 694 45. Chabrière, E. *et al.* Crystal structures of the key anaerobic enzyme pyruvate ferredoxin
695 oxidoreductase free and in complex with pyruvate. *Nat. Struct. Biol.* **6**, 182–190
696 (1999).
- 697 46. Volbeda, A. *et al.* Crystal structure of the nickel-iron hydrogenase from *Desulfovibrio*
698 *gigas*. *Nature* **373**, 580–587 (1995).
- 699 47. Martin, W. F. Carbon–metal bonds: rare and primordial in metabolism. *Trends*
700 *Biochem. Sci.* **44**, 807–818 (2019).
- 701 48. Buckel, W. & Thauer, R. K. Flavin-based electron bifurcation, ferredoxin, flavodoxin,
702 and anaerobic respiration with protons (Ech) or NAD⁺(Rnf) as electron acceptors: A
703 historical review. *Front. Microbiol.* **9**, (2018).
- 704 49. Vasiliadou, R., Dimov, N., Szita, N., Jordan, S. & Lane, N. Possible mechanisms of
705 CO₂ reduction by H₂ via prebiotic vectorial electrochemistry. *Interface Focus* (2018).
- 706 50. Kaufmann, M. On the free energy that drove primordial anabolism. *Int. J. Mol. Sci.* **10**,
707 1853–1871 (2009).
- 708 51. Patel, B. H., Percivalle, C., Ritson, D. J., Duffy, C. D. & Sutherland, J. D. Common
709 origins of RNA, protein and lipid precursors in a cyanosulfidic protometabolism. *Nat.*
710 *Chem.* **7**, 301–307 (2015).
- 711 52. Lane, N. & Martin, W. F. Perspective The Origin of Membrane Bioenergetics. *Cell*
712 **151**, 1406–1416 (2012).
- 713 53. Jordan, S. F., Nee, E. & Lane, N. Isoprenoids enhance the stability of fatty acid
714 membranes at the emergence of life potentially leading to an early lipid divide.
715 *Interface Focus* **9**, 20100067 (2019).
- 716 54. Jordan, S. F. *et al.* Promotion of protocell self-assembly from mixed amphiphiles at the
717 origin of life. *Nat. Ecol. Evol.* **3**, 1705–1714 (2019).
- 718 55. Kitadai, N. *et al.* Metals likely promoted protometabolism in early ocean alkaline
719 hydrothermal systems. *Sci. Adv.* **5**, eaav7848 19 (2019).
- 720 56. Muchowska, K. B. *et al.* Metals promote sequences of the reverse Krebs cycle. *Nat.*
721 *Ecol. Evol.* **1**, 1716–1721 (2017).
- 722 57. Lovley, D. R. & Phillips, E. J. Organic matter mineralization with reduction of ferric
723 iron in anaerobic sediments. *Appl. Environ. Microbiol.* **51**, 683–689 (1986).
- 724 58. Igarashi, K., Yamamura, Y. & Kuwabara, T. Natural synthesis of bioactive greigite by

- 725 solid – gas reactions. *Geochim. Cosmochim. Acta* **191**, 47–57 (2016).
- 726 59. Kato, S., Yumoto, I. & Kamagata, Y. Isolation of acetogenic bacteria that induce
727 biocorrosion by utilizing metallic iron as the sole electron donor. *Appl. Environ.*
728 *Microbiol.* **81**, 67–73 (2015).
- 729 60. Mayumi, D. *et al.* Carbon dioxide concentration dictates alternative methanogenic
730 pathways in oil reservoirs. *Nat. Commun.* **4**, 1–6 (2013).
- 731 61. Deng, X., Chan, C. K. & Tüysüz, H. Spent tea leaf templating of cobalt-based mixed
732 oxide nanocrystals for water oxidation. *ACS Appl. Mater. Interfaces* **8**, 32488–32495
733 (2016).
- 734 62. Yu, M., Moon, G., Bill, E. & Tüysüz, H. Optimizing Ni–Fe oxide electrocatalysts for
735 oxygen evolution reaction by using hard templating as a toolbox. *Appl. Energy Mater.*
736 **2**, 1199–1209 (2019).
- 737 63. Hanselmann, K. W. Microbial energetics applied to waste repositories. *Experientia* **47**,
738 645–687 (1991).
- 739 64. Amend, J. P. & Shock, E. L. Energetics of overall metabolic reactions of thermophilic
740 and hyperthermophilic archaea and bacteria. *FEMS Microbiol. Rev.* **25**, 175–243
741 (2001).
- 742 65. Wang, G., Spivack, A. J. & Hondt, S. D. Gibbs energies of reaction and microbial
743 mutualism in anaerobic deep subseafloor sediments of ODP Site 1226. *Geochim.*
744 *Cosmochim. Acta* **74**, 3938–3947 (2010).
- 745 66. Wagner, T., Ermler, U. & Shima, S. The methanogenic CO₂ reducing-and-fixing
746 enzyme is bifunctional and contains 46 [4Fe-4S] clusters. *Science* **354**, 114–117
747 (2015).
- 748 67. Mayumi, D. *et al.* Methane production from coal by a single methanogen. *Science* **354**,
749 222–225 (2016).
- 750 68. Hoffman, B. M. *et al.* Mechanism of nitrogen fixation by nitrogenase: the next stage.
751 *Chem. Rev.* **114**, 4041–62 (2014).

752